Journal of Materials Chemistry A

ROYAL SOCIETY OF CHEMISTRY

PAPER

View Article Online
View Journal

Cite this: DOI: 10.1039/d6ta01219a

Site-specific fluorination on donor–acceptor polymers enhances intramolecular charge transfer for photocatalytic hydrogen evolution

Wooteak Jung,†[a] Sanghyeok An, †[a] Gayoung Ham,†[b] Geoneop Choi,[a] Soyeon Lee,[c] Kyo Bin Park,[a] Jiwoong Yang, [cd] Dae Sung Chung *[a] and Hyojung Cha *[b]

The development of polymer photocatalysts remains a central challenge in achieving efficient solar-to-fuel conversion. A key limitation lies in the use of weak donor units, which hampers the optimization of intramolecular donor–acceptor interactions and reduces charge-transfer efficiency. Here, we report a site-specific fluorination strategy that addresses this bottleneck by introducing fluorine atoms at defined positions along the polymer backbone *via* a unique two-step polymerization protocol. Two representative random copolymers were synthesized: the acceptor-fluorinated polymer (PBF8BT-AF) and the donor-fluorinated polymer (PBF8BT-DF). Strikingly, PBF8BT-DF exhibited superior photocatalytic activity, while PBF8BT-AF showed inferior performance due to exciton loss through a non-productive decay pathway. A comprehensive spectroscopic analysis, supported by density functional theory (DFT) calculations, reveals that donor-site fluorination promotes exciton delocalization across the entire repeating unit, thereby facilitating efficient intramolecular charge transfer. In contrast, acceptor fluorination energetically localizes the excited state, impeding exciton migration and suppressing charge utilization. These findings underscore the critical role of site-specific exciton stabilization in determining photocatalytic efficiency and establish domain-targeted molecular engineering as a powerful design principle for next-generation polymer photocatalysts.

Received 9th February 2026
Accepted 30th May 2026

DOI: 10.1039/d6ta01219a

rsc.li/materials-a

Introduction

The transition to a sustainable energy system requires clean, high-density energy carriers, among which hydrogen is particularly promising due to its zero-emission operation and broad industrial applicability.[1] As interest in solar-driven hydrogen production continues to grow, the ability to rationally control photophysical processes has emerged as a central challenge.[2,3] While inorganic and hybrid photocatalysts have achieved impressive efficiencies, their optoelectronic properties are largely constrained by fixed crystal structures, offering limited flexibility in tailoring excited-state dynamics.[4,5] In contrast, organic conjugated polymers offer unique advantages, as their electronic structure, exciton behavior, and charge-transfer pathways can be systematically engineered at the molecular level through backbone and side-chain modification.[6–12] In particular, precise backbone design and chemical functionalization enable direct modulation of key parameters governing photocatalytic performance, such as intramolecular donor–acceptor interactions, exciton delocalization, and interfacial charge transfer.[13–18] This intrinsic design flexibility positions conjugated polymers as a versatile and promising class of materials for advancing solar fuel generation.

In general, the development of organic photocatalysts, particularly linear conjugated polymers, has been heavily influenced by the structural design principles and analytical methodologies originally established for organic photovoltaics (OPVs).[19] Recent progress has increasingly adopted alternating donor–acceptor (D–A) copolymer strategies from OPV materials to enhance intramolecular charge transfer (ICT).[20–22] However, a critical divergence exists between the two fields in the selection of donor units. In OPVs, strong electron-donating units are deliberately employed to enhance donor–acceptor hybridization, thereby broadening light absorption and strengthening ICT.[23,24] This strong electronic coupling facilitates the formation of charge transfer states that readily dissociate into free carriers, which can then be efficiently transported and extracted at the electrodes. From a device perspective, short-lived but highly mobile charge carriers are advantageous, as overall performance is governed by efficient charge transport and collection

[a]Department of Chemical Engineering, Pohang University of Science and Technology (POSTECH), Pohang 37673, Republic of Korea
[b]School of Energy Engineering, Kyungpook National University, 80 Daehak-ro, Buk-gu, Daegu 41566, Republic of Korea
[c]Department of Energy Science and Engineering, Daegu Gyeongbuk Institute of Science and Technology (DGIST), Daegu 42988, Republic of Korea
[d]Energy Science and Engineering Research Center, Daegu Gyeongbuk Institute of Science and Technology (DGIST), Daegu 42988, Republic of Korea
† Wooteak Jung, Sanghyeok An and Gayoung Ham contributed equally to this work.

rather than carrier lifetime.[25–27] In contrast, polymer photocatalyst systems have predominantly relied on weak donor units, such as fluorene or benzene.[28–30] Beyond synthetic convenience, this preference reflects fundamentally different kinetic requirements. In photocatalytic systems operating without external bias, charge carriers must persist long enough to participate in slow, multistep surface redox reactions at the polymer–cocatalyst–water interface, rather than being rapidly extracted. From this perspective, strong donor units—while effective in OPVs—can promote excessively fast charge delocalization and recombination, which are detrimental under catalytic conditions.[6,7] Consequently, weak donor units are empirically favored, as they suppress rapid charge extraction and enable the formation of long-lived excited states and charge carriers necessary to drive sluggish proton reduction reactions. This reliance on weak donors is further reinforced by synthetic constraints, as conventional cross-coupling strategies often limit the incorporation of monomers with highly mismatched reactivities. As a result of the distinct operating principles and synthetic challenges, the potential of strong donor units in polymer-based hydrogen evolution photocatalysts remains largely unexplored.

To address the synthetic challenges associated with constructing complex donor–acceptor molecular architectures, we previously developed a robust one-pot, two-step polymerization strategy that enables the precise integration of electronically disparate donor units within a single polymer backbone.[31] Using this approach, we successfully incorporated a strong electron-donating unit, benzodithiophene (BDT), alongside a weak donor, fluorene, to yield the PBF8BT-2 polymer. This material was specifically designed to probe donor-dependent charge dynamics in polymer photocatalysis and demonstrated high hydrogen evolution activity, establishing it as an ideal reference system for further molecular engineering. Building on this established synthetic versatility and well-defined electronic architecture, we now move toward site-specific molecular modification to further enhance photocatalytic performance. Among various chemical strategies, fluorination is particularly attractive due to its ability to modulate energy levels, dipole moments, and intramolecular charge distribution without introducing significant steric hindrance or disrupting the polymer backbone framework.[32–36] Furthermore, this approach is uniquely suited to our two-step polymerization protocol. While other electrophilic or nucleophilic substitutions, such as the introduction of ionic or highly polar side chains commonly used to tune wettability, can drastically alter the hydrophobic/hydrophilic balance of the monomers, fluorination maintains these macroscopic properties. Preserving this physicochemical similarity is crucial in our methodology to ensure consistent reactivity and strictly controlled incorporation ratios of the targeted domains. Therefore, fluorination provides the most reliable pathway to isolate purely electronic effects without compromising synthetic control. Importantly, PBF8BT-2 features spatially and functionally distinct domains: the BT–fluorene segment primarily governs exciton generation and suppresses recombination, while the BT–BDT domain serves as the terminal charge-accepting and catalytic site. This unique architecture provides a rare opportunity to selectively introduce fluorine at predefined donor or acceptor positions and directly compare their electronic consequences within a unified polymer system, while minimizing confounding effects from morphology or aggregation.

In this work, we focused on the distinct roles of the donor and acceptor units. Motivated by our previous findings highlighting the critical role of the BDT donor,[31] alongside the well-established significance of acceptor engineering in the literature,[37] we hypothesized that the position of halogenation would distinctively influence the photocatalytic behaviors. Guided by a targeted design strategy, we selectively introduced fluorine at either the acceptor (benzothiadiazole, BT) or donor (BDT) moiety, yielding two fluorinated derivatives: PBF8BT-AF and PBF8BT-DF, respectively. For the parent polymer, the donor monomer feed ratio of 0.75 : 0.25 (fluorene to BDT or FBDT) was deliberately selected based on their distinct physico-chemical roles. As demonstrated in our previous work,[31] while fluorene domains provide robust exciton generation, an excessively high BDT content induces an overly strong push–pull effect between the donor and acceptor units, which leads to severe exciton loss through non-radiative decay pathways. These site-specific modifications led to markedly divergent effects on photocatalytic performance. Fluorination of the acceptor in PBF8BT-AF induced a pronounced downshift in the BT energy levels, energetically localizing the excited state and disrupting exciton stabilization at the BT–BDT interface, which ultimately suppressed hydrogen evolution. In contrast, fluorination of the donor in PBF8BT-DF promoted exciton delocalization across the repeating unit, stabilized the excited state, and significantly extended charge carrier lifetimes. Density functional theory (DFT) calculations revealed that fluorination near the N=S=N group of the BT moiety downshifts the local dipole moment, shifting the exciton from a localized to a more delocalized electronic state. This enhanced delocalization improves ICT efficiency and, critically, enables more effective charge transfer to Pt cocatalysts under hole scavenging conditions. As a result, PBF8BT-DF exhibits up to a 50% increase in hydrogen evolution activity compared to the non-fluorinated PBF8BT-2. Collectively, these findings establish site-specific fluorination as a powerful molecular engineering strategy for conjugated polymer photocatalysts. By elucidating how selective fluorination at donor and acceptor moieties governs exciton generation, stabilization, and extraction, this study provides fundamental mechanistic insights and introduces a generalizable design principle for next-generation polymer-based materials for solar hydrogen evolution.

Results and discussion

Synthesis and characterization

To systematically examine the influence of fluorine substitution, the high-performing reference polymer PBF8BT-2 was selected as a well-defined parent structure. For clarity, PBF8BT-2 is hereafter referred to as PBF8BT throughout this work, and its fluorinated derivatives are denoted as PBF8BT-AF and PBF8BT-DF. This polymer features a precisely balanced combination of

weak (fluorene) and strong (BDT) donor units, providing an ideal molecular framework for probing donor- and acceptor-dependent charge dynamics in polymer photocatalysts. All polymers were synthesized using our previously developed two-step polymerization protocol,[31] which allows controlled incorporation of electronically disparate donor units within a single conjugated backbone. To minimize variations in optoelectronic properties arising from chain length effects, the number-average molecular weights (M_n) of all polymers were carefully tuned to approximately 8 kDa, ensuring that comparative studies reflect the intrinsic effects of site-specific fluorination rather than differences in molecular weight or dispersity. Importantly, the overall donor fraction was held constant across the series, ensuring that any observed differences in photophysical or photocatalytic behaviour arise primarily from site-specific fluorination rather than compositional variations. Within this controlled framework, fluorine atoms were selectively introduced at either the acceptor (benzothiadiazole, BT) or donor moiety to generate two derivatives: PBF8BT-AF, incorporating a fluorinated BT acceptor unit, and PBF8BT-DF, in which fluorination was confined to the BDT donor unit (Fig. 1a). Detailed synthetic procedures are provided in the SI.

The chemical structures of all polymers were confirmed by ^{1}H NMR spectroscopy, which exhibited characteristic resonances corresponding to both aromatic and alkyl protons, validating successful polymerization. All polymers showed good solubility in chloroform, ensuring compatibility with solution-based processing methods. Quantitative ^{1}H NMR analysis revealed BDT or BDTF incorporation ratios of 34% for PBF8BT-AF and 37% for PBF8BT-DF, closely matching the 33.8% content in PBF8BT. These values were determined based on the integration of α-proton signals from the side chains of BDT (3.2–2.8 ppm, in Fig. S1 and S2), as well as the α-proton of fluorene and the tertiary proton of the ethylhexyl side chain of BDT (2.2–1.9 ppm, in Fig. S1 and S2). These results confirm precise control over donor content within experimental error, underscoring the robustness of the two-step polymerization protocol. Beyond confirming the compositional accuracy, we further probed the local vibrational environments using FT-IR spectroscopy. The FT-IR spectra, obtained *via* the KBr pellet method to eliminate substrate interference, exhibit distinct site-dependent C–F vibrational features (Fig. S4). Aryl C–F stretching vibrations in conjugated polymers typically appear in the 1000–1400 cm^{-1} region.[38] In PBF8BT-AF, two relatively pronounced features appear in the 1250–1300 cm^{-1} region, which are consistent with C–F-related modes associated with the BT unit. Due to the electron-deficient nature of the BT moiety, coupling between the C–F stretching vibration and BT skeletal modes likely shifts these features toward relatively higher wavenumbers[33] within the fingerprint region. In contrast, PBF8BT-DF shows a broader band in the 1150–1200 cm^{-1} region, where C–F-related modes are strongly coupled with the highly delocalized backbone vibrations of the electron-rich thiophene (BDT) unit, resulting in broadened and less resolved spectral features.

To elucidate the molecular-level origin of the distinct photocatalytic behaviours induced by site-specific fluorination, we performed DFT calculations. Due to the computational complexity of modelling the full polymer backbone, representative monomer segments were employed, and electrostatic potential (ESP) mapping was used to capture local electronic perturbations induced by fluorine substitution (Fig. 1b). This approach is particularly effective for resolving changes in local dipole moments and charge redistributions that govern exciton stabilization and ICT. For the acceptor-fluorinated derivative PBF8BT-AF, DFT calculations revealed that fluorine substitution on the BT unit does not reverse the intrinsic dipole moment, contrary to our initial expectation. Instead, fluorination significantly stabilizes the energy level of the intermediate BT–Flu segment. As this segment acts as an energetic bridge along the intramolecular charge transport pathway, its over-stabilization effectively flattens the energetic landscape between the BT–Flu and downstream BT–BDT domains. This reduction in the energetic gradient diminishes the thermodynamic driving force for charge migration toward the terminal charge-accepting site, thereby impeding charge transfer kinetics and explaining the experimentally observed suppression of hydrogen evolution activity. In contrast, donor fluorination in PBF8BT-DF generates a markedly different electronic environment. Here, the fluorine atom is positioned opposite the electron-rich N=S=N group of the BT moiety. DFT calculations show that this configuration reverses the local dipole orientation of the BT unit; notably, the new dipole vector extends vertically rather than being confined along the N=S=N bond axis. This three-dimensional redistribution of charge density enhances exciton stabilization and reduces localization-driven non-radiative decay. As a result, PBF8BT-DF exhibits more robust charge carrier delocalization across the BT–BDT interface.

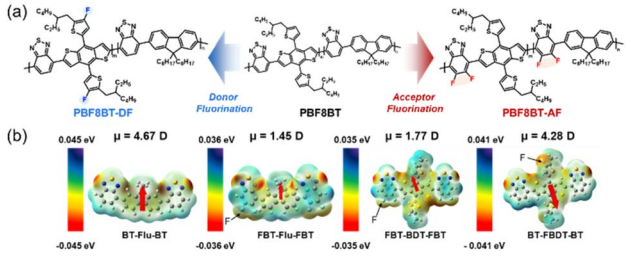

Fig. 1 (a) Schematic illustration of the polymer photocatalyst design and synthetic strategy, (b) electrostatic potential maps and calculated dipole moments of the monomer units BT-Flu, FBT-Flu, FBT-BDT, and BT-FBDT.

Optical and electronic properties

The UV-vis absorption spectra (Fig. 2b) of the conjugated polymers were investigated using polymer dots (Pdots) prepared *via* nanoprecipitation and dispersed in distilled water, stabilized with poly(styrene)-*co*-poly(ethylene glycol)-*co*-poly(carboxylic acid) (PS–PEG–COOH).[39,40] This Pdot-based approach minimizes aggregation-induced spectral distortion, allowing reliable comparison with the solid-state polymers. Compared with the reference PBF8BT, PBF8BT-AF exhibited a distinct blue shift in

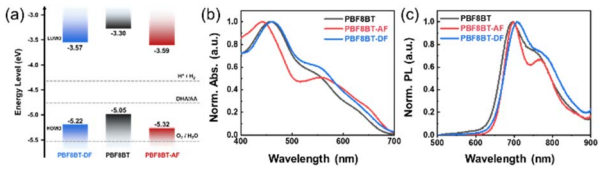

Fig. 2 (a) Energy level diagram of PBF8BT-DF, PBF8BT, and PBF8BT-AF. Dashed lines indicate the proton reduction potential (H^+/H_2). (b) UV-visible absorption spectra and (c) photoluminescence spectra of Pdots dispersions in water.

the main absorption peak, from 456 nm to 440 nm, while PBF8BT-DF showed a negligible spectral shift in the short-wavelength region. These results support the hypothesis that absorption in the 400–500 nm range is primarily governed by the BT–Flu domain, which remains largely unaffected by donor-site fluorination. In contrast, both fluorinated derivatives displayed clear red shifts at longer wavelengths, indicative of reduced optical bandgaps due to enhanced π-delocalization and local electronic perturbations from fluorine substitution. Among them, PBF8BT-AF showed the most pronounced red shift, suggesting that direct fluorination on the BT acceptor more effectively perturbs backbone conjugation than donor-side substitution.

Photoluminescence (PL) spectra (Fig. 2c), recorded under the same Pdots water-dispersed conditions as the UV-vis measurements, revealed that all fluorinated polymers exhibited red-shifted emission relative to PBF8BT, indicating reduced energy gaps between the excited and ground states. Notably, PBF8BT-DF showed the largest red shift, attributed to donor-site fluorination enhancing ICT. This modification extends the effective conjugation length and redistributes frontier molecular orbitals, thereby stabilizing the excited state more efficiently than acceptor-side fluorination. These findings highlight the BT–BDT domain as the terminal exciton-accepting site, with donor fluorination further reinforcing its role in exciton stabilization.

Ultraviolet photoelectron spectroscopy (UPS) was employed to determine the highest occupied molecular orbital (HOMO) energy levels of the conjugated polymers. Both fluorinated polymers exhibited a clear downshift in HOMO levels relative to PBF8BT, with the strongest stabilization observed for PBF8BT-AF, consistent with the stronger electron-withdrawing effect of BT-site fluorination. Optical bandgaps (E_{opt}), extracted from Tauc plots, were used in conjunction with UPS-derived HOMO values to estimate the lowest unoccupied molecular orbital (LUMO) levels. Complementary cyclic voltammetry (CV) measurements revealed similar trends, although the magnitude of the HOMO downshift was less pronounced than that observed by UPS. Despite minor discrepancies in absolute values, both methods consistently demonstrated fluorination-induced stabilization of the frontier orbitals. A comprehensive summary of the thermal, optical, and electronic properties is presented in Tables 1, S1 and Fig. S5, S6.

Photocatalytic hydrogen evolution performance

To characterize the colloidal properties of the Pdots was employed to determine hydrodynamic radii, while nanoparticle tracking analysis (ZetaView® ×30) was used to assess morphology. Across the series of conjugated polymers, the Pdots exhibited hydrodynamic radii centered around ~100 nm (Fig. S7), consistent with well-dispersed nanoscale colloids suitable for photocatalytic evaluation.

Photocatalytic hydrogen evolution rates (HERs) of the Pdots were quantified under simulated solar illumination (300 W Xe lamp, 100 mW cm^{-2}, AM 1.5G), using ascorbic acid (AA, pH = 4, NaOH-buffered) as a sacrificial electron donor. As shown in Fig. 3a, the fluorinated donor derivative PBF8BT-DF significantly outperformed its counterparts in the absence of a cocatalyst, achieving an average HER of 10 250 μmol g^{-1} h^{-1}. This represents a substantial enhancement over both the non-fluorinated PBF8BT (7340 μmol g^{-1} h^{-1}) and the acceptor-fluorinated PBF8BT-AF (5120 μmol g^{-1} h^{-1}). Upon deposition of 10 wt% Pt as a cocatalyst (using K_2PtCl_6), HERs increased across all polymers, while the performance trend remained consistent: PBF8BT-DF achieved a remarkable HER of 31 000 μmol g^{-1} h^{-1}, outperforming PBF8BT (22 000 μmol g^{-1} h^{-1}) and PBF8BT-AF (15 180 μmol g^{-1} h^{-1}).

To evaluate the robustness of these trends, AA was replaced with 30 v/v% triethanolamine (TEOA, pH = 10, HCl-buffered) as the sacrificial electron donor. Although absolute HER values changed, the relative performance order among the polymers remained unchanged (PBF8BT-DF: 18 000 μmol g^{-1} h^{-1}, PBF8BT: 13 200 μmol g^{-1} h^{-1}; PBF8BT-AF: 9100 μmol g^{-1} h^{-1}, with 10 wt% Pt cocatalysts) (Fig. 3b). This consistency confirms that the superior activity of donor-fluorinated PBF8BT-DF arises from intrinsic molecular properties rather than dependence on a specific hole scavenger. Collectively, these results reveal a clear structure–activity relationship: fluorination at the donor (BDT) moiety markedly enhances photocatalytic performance, whereas fluorination at the acceptor (BT) moiety diminishes it. Relative to its non-fluorinated analogue, PBF8BT-DF demonstrated 1.4-fold (without Pt) and 1.9-fold (with Pt) increases in HER, while PBF8BT-AF consistently underperformed. This divergent behaviour underscores the directional impact of selective backbone fluorination, which benefits electron-donating segments but disrupts the electronic structure of electron-accepting units.

The long-term operational stability of the optimized PBF8BT-DF Pdots was further evaluated (Fig. 3c). After each 5 h photocatalytic cycle, the system was purged with high-purity argon (>99.99%) and replenished with ascorbic acid to prevent electron donor depletion. The other polymers (PBF8BT-AF and PBF8BT) also showed consistent photocatalytic performance over three cycles. Liquid-Phase Transmission Electron Microscopy (LP-TEM) characterization (Fig. S8) of the spent catalysts further demonstrated that the initial morphology of the Pdots was preserved after the reaction. This evidence suggests that the chemical and physical structures of the polymer nanoparticles remain stable during the photocatalytic hydrogen evolution process. In addition, the chemical stability of the Pdots was

Table 1 Thermal, optical, and electrochemical properties of the synthesized conjugated polymers

Polymers	M_n[a] [kg mol^{-1}]	PDI	T_d[b] [°C]	λ_{max} [nm]	λ_{edge} [nm]	E_g^{optc} [eV]	LUMO[d] [eV]	HOMO[e] [eV]
PBF8BT-AF	8.4k	1.94	340	440	694	1.73	−3.59	−5.32
PBF8BT-DF	7.6k	2.19	391	461	692	1.65	−3.57	−5.22

[a] Determined by gel permeation chromatography (GPC) using tetrahydrofuran as an eluent at 40 °C, relative to a polystyrene standard. [b] Thermal decomposition temperature (5% weight loss) determined by TGA under N_2. [c] Optical band gap estimated from the absorption edges (λ_{edge}) in the solution state. [d] Lowest unoccupied molecular orbital (LUMO) levels were estimated from the onset of the first reduction potentials with reference to ferrocene at −4.8 eV. [e] HOMO = LUMO + E_g^{opt}.

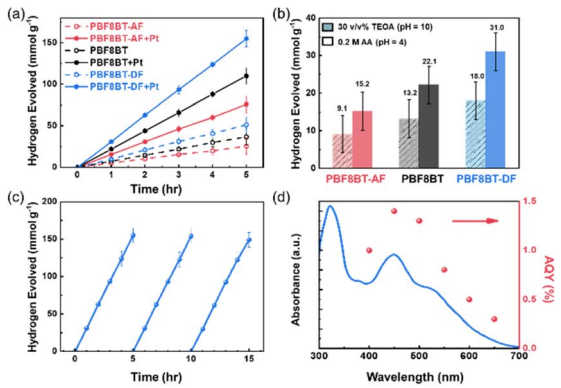

Fig. 3 (a) Comparison of HERs for PBF8BT derivatives with and without photo-deposited Pt cocatalysts (10 wt%) in ascorbic acid (AA, pH = 4) under visible light irradiation (λ > 420 nm). (b) Average HERs over 5 h for each sample across five repeated runs, demonstrating reproducibility using AA and triethanolamine (TEOA 30 v/v%, pH = 10, HCl-buffered) as sacrificial agents. (c) Photocatalytic stability of optimized PBF8BT-DF Pdots over three consecutives 5 h cycles. (d) Apparent quantum yield (AQY) of PBF8BT-DF at 400, 420, 450, 500, and 550 nm, shown alongside the absorbance spectrum of 0.2 M AA (pH = 4).

evaluated by comparing the UV-vis absorption spectra before and after the photocatalytic process. No discernible changes in the spectral profiles were observed for PBF8BT-AF, PBF8BT, and PBF8BT-DF (Fig. S9), indicating that the conjugation length and structural integrity of the polymers remain intact during the hydrogen evolution tests. Under these conditions, PBF8BT-DF retained approximately 95% of its initial activity over three consecutive runs, demonstrating excellent photostability. Apparent quantum yield (AQY) measurements (Fig. 3d) showed efficiencies of 1.4% at 450 nm and 0.3% at 350 nm, consistent with previous findings that PBF8BT-DF exhibits ~1.3-fold higher AQY than PBF8BT at 450 nm. To rule out the influence of residual palladium from polymer synthesis on photocatalytic performance, inductively coupled plasma (ICP) analysis was performed on all polymers (Table S2). The Pd content was comparable across the series, confirming that residual catalyst contamination was not a determining factor.

Finally, we considered the potential influence of polymer surface wettability (Fig. S10) to determine whether the fluorination induced any significant extrinsic changes,[41] particularly regarding Pdots morphology in aqueous media. The contact angle measurements revealed that both the donor- and acceptor-fluorinated derivatives exhibit wettability comparable to that of PBF8BT, with only negligible variations. These results suggest that fluorination does not significantly alter the macroscopic hydrophilicity or the morphology of the Pdots. Consequently, we can posit that differences in wettability and morphological features are not the primary drivers of the observed performance enhancement. This allows us to attribute the improved hydrogen evolution primarily to intrinsic electronic and photophysical modifications, which are comprehensively analyzed in the following section.

Photophysical study of photocatalysts

To complement these theoretical insights, we conducted time-resolved PL (TR-PL) measurements across the polymer series, both in pristine form and in the presence of cocatalysts or sacrificial agents (Fig. 4a and b). The TR-PL data revealed that both PBF8BT-AF and PBF8BT-DF exhibit shortened lifetimes on the order of a few nanoseconds (Tables S3 and S4), indicating efficient exciton dissociation. This suggests that initial charge separation within the conjugated backbone is not the sole determinant of photocatalytic activity. However, a closer inspection revealed critical differences in the fate of these excitons. Analysis of emission-lifetime spectra showed that site-specific fluorination significantly influences exciton behaviour. For PBF8BT-AF, exciton lifetimes were particularly short at emission wavelengths of 680 nm and 700 nm, suggesting that fluorination at the BT unit facilitates rapid exciton quenching. While this may enhance internal charge separation, the quenching appears to be predominantly non-productive,

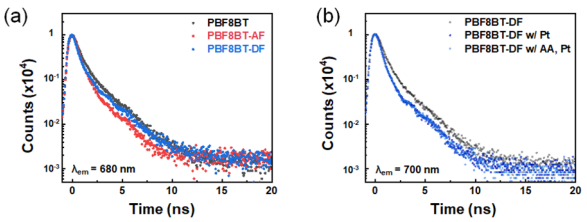

Fig. 4 (a) TR-PL decay curves of PBF8BT (black), PBF8BT-AF (red), and PBF8BT-DF (blue) Pdots measured at an emission wavelength of 680 nm. Both fluorinated derivatives exhibit shorter exciton lifetimes than the non-fluorinated reference, indicating enhanced exciton quenching upon fluorination. (b) TR-PL decay profiles of PBF8BT-DF Pdots, Pt-photodeposited DF Pdots, and DF Pdots in the presence of ascorbic acid (AA) under excitation at 450 nm.

channeling excitons into non-radiative decay pathways that limit hydrogen evolution. Thus, although AF substitution promotes exciton dissociation, it does not translate into improved photocatalytic efficiency. In contrast, PBF8BT-DF exhibited a more pronounced reduction in PL lifetime upon cocatalyst deposition, directly linking exciton quenching to interfacial charge transfer rather than intramolecular decay. Furthermore, under Pt cocatalyst and AA conditions (Fig. S11), internal excitons in Pdots remained observable, and their lifetimes were further reduced, indicating efficient carrier transfer at the polymer–cocatalyst interface. This behaviour underscores a central mechanistic point: while both AF and DF substitutions facilitate exciton dissociation, only DF effectively directs this process toward productive charge transfer, thereby enabling higher hydrogen evolution activity.

Overall, the combined DFT and TR-PL results establish that the decisive factor for photocatalytic efficiency is not exciton dissociation alone, but rather the subsequent stabilization and extraction of charges at the polymer–cocatalyst interface. Among the series, the donor-fluorinated PBF8BT-DF uniquely fulfills these criteria, thereby accounting for its superior performance relative to both its non-fluorinated and acceptor-fluorinated analogues.

To further elucidate the role of site-specific fluorination, nanosecond transient absorption spectroscopy (ns-TAS) was performed on PBF8BT-based Pdots to probe their carrier dynamics. Our previous study,[31] demonstrated that optimized BDT incorporation in pristine PBF8BT facilitates long-lived charge separated states by suppressing both radiative and non-radiative recombination, thereby enabling efficient charge transfer to cocatalysts and enhanced photocatalytic hydrogen evolution. Building upon this, the present study examines how site-specific fluorination further modulates these dynamics in PBF8BT, PBF8BT-AF, and PBF8BT-DF. Pristine PBF8BT was used as a direct reference to evaluate fluorination-induced changes in excited state behaviour. The TA spectra display ground-state bleach (GSB) features at ~470 nm, attributed to the BT unit, and the 580–600 nm range, associated with the BDT segment (Fig. 5a and b). In the pristine PBF8BT, the coexistence of BT- and BDT-related excited states is evidenced by the clear GSB features at both 470 and 580 nm, while a photoinduced absorption (PIA) signal is observed at 720 nm (Fig. S12). Although the overall spectral profiles remain similar across the Pdots, the relative intensities and kinetic behaviours of the GSB signals diverge significantly upon site-specific fluorination. For PBF8BT-AF, the GSB at 470 nm becomes markedly pronounced, suggesting that fluorination of the BT unit modulates the excited-state population associated with BT-centered transitions. PBF8BT-DF, on the other hand, shows a strengthened GSB at 580 nm, indicating that fluorination on the BDT unit enhances the contribution of BDT-centered excited states.

The relaxation kinetics further elucidate the dynamics of these photogenerated carriers (Fig. 5c, d and Table S5). The notably slowed GSB recovery at 470 nm in PBF8BT-AF suggests that fluorination at the BT unit stabilizes localized excited states by suppressing rapid recombination. The intensified and prolonged GSB response further implies the formation of BT-centered trapped states. However, this extended lifetime likely corresponds to a localized excited state that does not efficiently contribute to productive interfacial charge transfer, thus limiting its photocatalytic contribution. In contrast, PBF8BT-DF exhibits more persistent GSB dynamics at 580 nm, indicating the efficient funneling of excited state carriers into long-lived charges associated with the BDT domain. This reflects a comparatively more productive excited-state relaxation process that facilitates interfacial charge transfer. Such behaviour is consistent with more efficient intermolecular carrier migration. Regarding the PIA features at 720 nm (Table S6), the decay kinetics vary with the fluorination site. Pristine PBF8BT shows the slowest decay, likely due to more delocalized charge carriers in the absence of fluorination. The accelerated decay in PBF8BT-DF is consistent with a charge-transfer-assisted carrier relaxation pathway, potentially associated with more efficient intermolecular carrier migration. In contrast, PBF8BT-AF exhibits intermediate behaviour, where localized relaxation pathways potentially compete with productive charge separation.

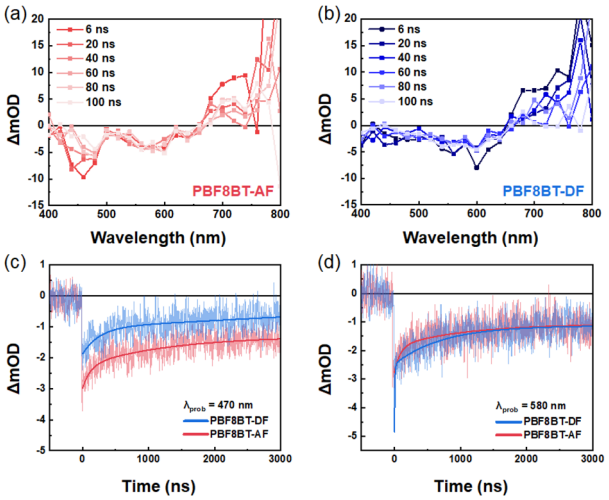

Fig. 5 ns-TAS analyses of PBF8BT-AF and PBF8BT-DF Pdots. Transient absorption spectra of (a) PBF8BT-AF and (b) PBF8BT-DF Pdots. (c) GSB kinetics probed at 470 nm, corresponding to the BT unit, for both samples. (d) GSB kinetics probed at 580 nm, assigned to the BDT segment, for AF and DF Pdots. All measurements were conducted with excitation at 355 nm and a fluence of 2 mJ cm^{-2}. Polymer suspensions were prepared to have an absorbance of 0.42 at 355 nm and were thoroughly purged with argon before measurement.

To validate the correlation between these dynamics and photocatalytic performance, we evaluated the representative PBF8BT-DF system under operative conditions (with AA and Pt). Consistent with the reduced exciton lifetimes observed in TRPL (Fig. S11), the TAS analysis provides direct evidence for efficient carrier extraction (Fig. S13 and Table S7). The marked decrease in initial ΔOD amplitudes (Fig. S13a–d) and the accelerated decay kinetics (Fig. S13e and f) in the presence of the cocatalyst confirm that photogenerated carriers are rapidly extracted to the Pt interface to participate in catalytic redox reactions. Overall, the integrated analysis of TRPL and TAS confirms that

DF substitution promotes an optimized interfacial charge transfer, leading to the observed enhancement in hydrogen evolution.

Based on our comprehensive analysis, the superior photocatalytic performance of PBF8BT-DF is attributed to the strategic fluorination on the donor moiety, as shown in Fig. 6. This modification effectively reorients the local dipole moment, resulting in three-dimensional stabilization and delocalization of the electron density across the polymer backbone. Such stabilization not only prolongs the exciton lifetime but also efficiently channels charges to the low-energy BT-BDT domains. In photocatalytic systems, this suggests that preserving the structural integrity of the BT unit—without modifications such as fluorination—plays a more favorable role in enhancing photocatalytic activity. Ultimately, this leads to more effective charge transfer to the cocatalyst, which is the critical factor in achieving a significantly higher HER compared to other derivatives.

Conclusions

In this study, we systematically investigated the synthesis, optoelectronic properties, and photocatalytic hydrogen-evolution performance of PBF8BT-based conjugated polymers with site-selective fluorine modification. Using a robust two-step polymerization strategy, we precisely introduced fluorine atoms onto either the acceptor or donor moiety, yielding two structurally well-defined derivatives: PBF8BT-AF and PBF8BT-DF. Our results demonstrate that photocatalytic activity is highly sensitive to the fluorination site. While fluorination of the acceptor unit in PBF8BT-AF suppresses hydrogen evolution, donor fluorination in PBF8BT-DF markedly enhances it, achieving a maximum HER of 31 000 μmol g^{-1} h^{-1}. Through comprehensive photophysical characterization and DFT analyses, we show that this contrasting behaviour arises not from differences in initial exciton generation, but from fundamentally distinct exciton stabilization pathways. Although both fluorinated polymers exhibit efficient exciton dissociation, only donor-side fluorination enables productive stabilization of the excited state. Specifically, fluorination at the donor moiety induces reorientation of the local dipole moment, promoting exciton delocalization across the repeating unit, suppressing non-radiative decay, and prolonging charge-carrier lifetimes. This stabilized and delocalized excited state facilitates efficient charge transfer to the cocatalyst, ultimately resulting in superior photocatalytic performance. These findings underscore the critical role of domain-specific molecular engineering in conjugated polymer photocatalysts and demonstrate that exciton dissociation alone is insufficient to ensure high catalytic efficiency. Instead, the ability to stabilize and direct photogenerated charges toward productive interfacial pathways is the key determinant. More broadly, this work establishes site-selective fluorination as a powerful and promising design strategy for modulating exciton dynamics and charge utilization, providing clear molecular-level guidelines for developing next-generation polymer-based photocatalysts for solar hydrogen evolution.

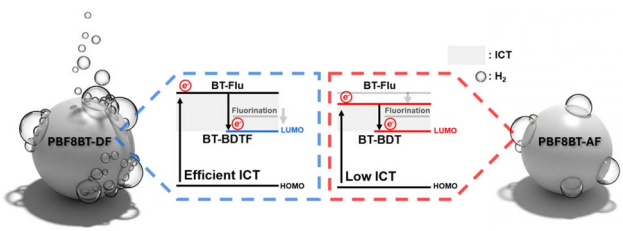

Fig. 6 Schematic illustration of the photocatalytic processes in PBF8BT-DF and PBF8BT-AF Pdots.

Author contributions

W. J. synthesized the materials and wrote the manuscript. S. A. tested the catalyst performance and edited the manuscript. G. H. measured the photophysics of the materials and edited the manuscript. G. C. performed the DFT calculations. J. Y. and S. L. measured TEM. K. B. measured FT-IR. D. C., and H. C., edited and supervised the manuscript. The authors appreciate the Pohang Accelerator Laboratory (PAL) for providing the 4D and 10A2 beamlines used in this study.

Conflicts of interest

There are no conflicts to declare.

Data availability

The data supporting the findings of this study are available within the article and its supplementary information (SI). Supplementary information: all relevant characterization data, including NMR, TGA, FT-IR for the polymers and DLS, LP-TEM for the Pdots. See DOI: https://doi.org/10.1039/d6ta01219a.

Acknowledgements

This work was supported by the National Research Foundation of Korea (NRF) grant funded by the Korea government (MSIT) (RS-2023-00213920), Basic Science Research Program through the National Research Foundation of Korea (NRF) funded by the Ministry of Education (RS-2025-25400520) and the Korea Institute for Advancement of Technology (KIAT) through the International Cooperative R&D Program (P0026257). The UPS measurement was performed at 4D and 10A2 beamline of the Pohang Accelerator Laboratory (PAL) in Republic of Korea.

References

1 A. Fujishima and K. Honda, *Nature*, 1972, **238**, 37–38.
2 H. Lim, N. I. Kim, G. Shin, J. Lee, S. Kim, S. W. Myeong, C. Kim, S. M. Choi and T. Park, *Adv. Energy Mater.*, 2025, **15**, 2570106.
3 H. Lim, J.-Y. Jeong, D. H. Lee, S.-W. Myeong, G. Shin, D. Choi, W. B. Kim, S. M. Choi and T. Park, *J. Mater. Chem. A*, 2023, **11**, 25938–25944.

4 S. Singh, Z. Hamid, R. Babu, S. Gómez-Graña, X. Hu, I. McCulloch, R. L. Hoye, V. Govind Rao and L. Polavarapu, *Adv. Mater.*, 2025, 2419603.
5 J. Wang, M. Zhang, Z. Chen, L. Li, G. Jiang and Z. Li, *ACS Energy Lett.*, 2024, **9**, 653–661.
6 J. Choi, W. Jung, S. Gonzalez-Carrero, J. R. Durrant, H. Cha and T. Park, *Energy Environ. Sci.*, 2024, **17**, 7999–8018.
7 W. Jung, J. Choi, S. An, S. Yun, D. S. Chung, H. Cha, J. Lim and T. Park, *Adv. Energy Mater.*, 2025, **15**, 2501600.
8 C.-L. Chang, W.-C. Lin, L.-Y. Ting, C.-H. Shih, S.-Y. Chen, T.-F. Huang, H. Tateno, J. Jayakumar, W.-Y. Jao and C.-W. Tai, *Nat. Commun.*, 2022, **13**, 5460.
9 M. Yu, W. Zhang, Z. Guo, Y. Wu and W. Zhu, *Angew. Chem., Int. Ed.*, 2021, **60**, 15590–15597.
10 C.-J. Wu, T.-R. Li, W.-J. Liang, H.-J. Wang, L.-J. Niu, J. Fan, J.-L. Kan, Y. Geng and Y.-B. Dong, *Nat. Commun.*, 2026, **17**, 3028.
11 L. Zhang, C. Wang, Q. Jiang, P. Lyu and Y. Xu, *J. Am. Chem. Soc.*, 2024, **146**, 29943–29954.
12 X. Li, Y. Wang, L. Cheng and L. Liu, *Adv. Mater.*, 2026, e23654.
13 C. Dai, S. Xu, W. Liu, X. Gong, M. Panahandeh-Fard, Z. Liu, D. Zhang, C. Xue, K. P. Loh and B. Liu, *Small*, 2018, **14**, 1801839.
14 P. Chen, C. Ru, L. Hu, X. Yang, X. Wu, M. Zhang, H. Zhao, J. Wu and X. Pan, *Macromolecules*, 2023, **56**, 858–866.
15 P. Chen, F. Ji, D. Ma, Y. Xie, X. Wu, M. Zhang, C. Ru, L. Zhou, J. Wu and X. Pan, *J. Mater. Chem. A*, 2023, **11**, 21146–21152.
16 B. Chen, B. Li, Y. Su, J. Zhu, M. Gao, S. Xiong, P. Wang, Z. Wang, Q. Liao and C. Gu, *Angew. Chem.*, 2025, **137**, e202515924.
17 B. Lin, D. H. Si, J. J. Li, S. Y. Gao, X. Yang and R. Cao, *Adv. Mater.*, 2026, e20022.
18 C. Li, P. Chen, Y. Zhang, Y. X. Ye, G. Ouyang and L. Guo, *Angew. Chem., Int. Ed.*, 2026, e20573.
19 J. Hou, O. Inganäs, R. H. Friend and F. Gao, *Nat. Mater.*, 2018, **17**, 119–128.
20 Y. Liang, Z. Xu, J. Xia, S.-T. Tsai, Y. Wu, G. Li, C. Ray and L. Yu, *Adv. Mater.*, 2010, **22**, E135.
21 H. Zhou, L. Yang and W. You, *Macromolecules*, 2012, **45**, 607–632.
22 N. Blouin, A. Michaud, D. Gendron, S. Wakim, E. Blair, R. Neagu-Plesu, M. Belletete, G. Durocher, Y. Tao and M. Leclerc, *J. Am. Chem. Soc.*, 2008, **130**, 732–742.
23 H. Yao, L. Ye, H. Zhang, S. Li, S. Zhang and J. Hou, *Chem. Rev.*, 2016, **116**, 7397–7457.
24 C. Han, J. Wang, S. Zhang, L. Chen, F. Bi, J. Wang, C. Yang, P. Wang, Y. Li and X. Bao, *Adv. Mater.*, 2023, **35**, 2208986.
25 D. Bartesaghi, I. D. C. Pérez, J. Kniepert, S. Roland, M. Turbiez, D. Neher and L. J. A. Koster, *Nat. Commun.*, 2015, **6**, 7083.
26 S. R. Cowan, N. Banerji, W. L. Leong and A. J. Heeger, *Adv. Funct. Mater.*, 2012, **22**, 1116–1128.
27 P. Bi, S. Zhang, J. Wang, J. Ren and J. Hou, *Chin. J. Chem.*, 2021, **39**, 2607–2625.
28 R. S. Sprick, B. Bonillo, R. Clowes, P. Guiglion, N. J. Brownbill, B. J. Slater, F. Blanc, M. A. Zwijnenburg, D. J. Adams and A. I. Cooper, *Angew. Chem., Int. Ed.*, 2016, **55**, 1792–1796.
29 X.-H. Zhang, X.-P. Wang, J. Xiao, S.-Y. Wang, D.-K. Huang, X. Ding, Y.-G. Xiang and H. Chen, *J. Catal.*, 2017, **350**, 64–71.
30 D. J. Woods, S. A. Hillman, D. Pearce, L. Wilbraham, L. Q. Flagg, W. Duffy, I. McCulloch, J. R. Durrant, A. A. Guilbert and M. A. Zwijnenburg, *Energy Environ. Sci.*, 2020, **13**, 1843–1855.
31 W. Jung, S. An, G. Ham, C. Kim, S. Lee, J. Yang, D. S. Chung, H. Cha and T. Park, *EES Catal.*, 2025, **3**, 775–782.
32 X. Tu, X. Yao, Y. Li, S. Zhang, Z. He, C. Zhang, Z. Liu, H. Zhong and Z. Fei, *ACS Appl. Polym. Mater.*, 2024, **6**, 5970–5979.
33 Y. Xiang, X. Wang, L. Rao, P. Wang, D. Huang, X. Ding, X. Zhang, S. Wang, H. Chen and Y. Zhu, *ACS Energy Lett.*, 2018, **3**, 2544–2549.
34 K. Tu, Y. Chen, T. Duan, S. Duan, D. Hu, L. Liu, G. Tian, T. Gu, H. Liu and X. Lu, *Adv. Funct. Mater.*, 2025, e11914.
35 X. Kang, X. Li, H. Liu, Z. Liang, W. Chen, N. Zheng, S. Qiao and R. Yang, *ACS Appl. Mater. Interfaces*, 2020, **12**, 49849–49856.
36 L. Benatto and M. Koehler, *J. Phys. Chem. C*, 2019, **123**, 6395–6406.
37 H. Yu, Y. Wang, X. Zou, H. Han, H. K. Kim, Z. Yao, Z. Wang, Y. Li, H. M. Ng and W. Zhou, *Adv. Funct. Mater.*, 2023, **33**, 2300712.
38 S. S. Nair, B. R. Isaac, S. Alwarappan, S. Sreedeep and V. K. Pillai, *ACS Appl. Nano Mater.*, 2024, **7**, 7337–7344.
39 P. B. Pati, G. Damas, L. Tian, D. L. A. Fernandes, L. Zhang, I. B. Pehlivan, T. Edvinsson, C. M. Araujo and H. Tian, *Energy Environ. Sci.*, 2017, **10**, 1372–1376.
40 M. V. Pavliuk, S. Wrede, A. Liu, A. Brnovic, S. Wang, M. Axelsson and H. Tian, *Chem. Soc. Rev.*, 2022, **51**, 6909–6935.
41 S. Lee, J.-S. Park and T. R. Lee, *Langmuir*, 2008, **24**, 4817–4826.

